

Point-Wise Wind Retrieval and Ambiguity Removal Improvements for the QuikSCAT Climatological Data Set

Alexander G. Fore, Bryan W. Stiles, Alexandra H. Chau, Brent A. Williams, R. Scott Dunbar, and Ernesto Rodríguez

Abstract—In this paper, we introduce a reprocessing of the entire SeaWinds on QuikSCAT mission. The goal of the reprocessing is to create a climate data record suitable for climate studies and to incorporate recent algorithm improvements. Three different levels of QuikSCAT data are produced at the Jet Propulsion Laboratory: L1B, geolocated, calibrated, backscatter measurements in chronological order by acquisition time; L2A, backscatter measurements binned into a geographical grid; and L2B, gridded ocean surface wind vectors. This reprocessing only changes the L2A and L2B data; we have not changed the L1B processing at all. We introduce new algorithms used in the L1B to L2A processing and in the L2A to L2B processing. After introducing our new algorithms, we show the validation studies performed to date, which include comparisons to numerical weather products, comparisons to buoy data sets, comparisons to other remote sensing instruments, and spectral considerations.

Index Terms—Ocean winds, radar, rain, remote sensing, scatterometry.

I. INTRODUCTION

SEAWINDS on QuikSCAT was designed with the primary mission to measure ocean surface vector winds (OVWs). QuikSCAT is a microwave scatterometer, which measures the ocean surface roughness at Ku-Band (13.4 GHz/2.24 cm). SeaWinds on QuikSCAT obtained global coverage of ocean surface winds for over a decade from its launch in 1999 until November 2009. With more than a decade of observations, we have been working with the International Ocean Vector Winds Science Team to reprocess the QuikSCAT data for use in climate studies. OVW is a critical variable in many geophysical studies, and QuikSCAT was able to observe 93% of the ocean surface daily. QuikSCAT provides a rich data set not only due to the ten years of continuous data but also due to the myriad of applications, namely, ice monitoring [1], soil moisture [2], freeze thaw [3], and snow [4], in addition to OVW.

This reprocessing includes many significant improvements. The previous high-resolution 12.5-km data product (hereafter referred to as V2L2B12) [5] was noisy and contained many wind vector cells (WVCs) lacking enough measurements for wind retrieval due to sampling limitations in particular regions of the swath. In addition, both 12.5- and 25-km V2 data products contained significant rain contamination [6] and had

noisy direction retrievals due to insufficient filtering. The new (V3L2B12) processing overcomes many of these shortcomings and uses a new model function developed by Remote Sensing Systems [7]. In Fig. 1, we plot the speed (in gray scale) and direction (as arrows) for the V2 products [see Fig. 1(b) and (c)], the V3L2B12 product [see Fig. 1(a)], and European Centre for Medium-Range Weather Forecasts (ECMWF) [see Fig. 1(d)] for comparison. The V3L2B12 product [see Fig. 1(a)] shows much less noise in the speed and direction than the previous V2L2B12 product [see Fig. 1(b)] and has less noise than the previous V2 L2B25 product [see Fig. 1(c)]. The missing WVCs in Fig. 1(b) are completely restored in Fig. 1(a), and the regions of rain contamination in Fig. 1(b) and (c) have been significantly reduced in the V3L2B12 product [see Fig. 1(a)].

Scatterometers are microwave radars that measure the normalized radar backscatter cross-section (σ_0). Empirical and theoretical geophysical model functions (GMFs) have been extensively developed for the radar cross section as a function of the equivalent neutral wind speed and direction at 10-m height, incidence angle, relative azimuth angle, radar wavelength, and polarization [8]–[13]. In Fig. 2, we plot the GMF as a function of relative azimuth angle for different wind speeds. From this figure, it is clear that the one scatterometer measurement is not sufficient to determine the wind speed and direction. Typically, four observations from different relative azimuth angles are needed to determine the wind speed and direction. QuikSCAT achieves the required observations by using two different conically scanning antenna beams, namely, an H-polarized inner beam at 46° and a V-polarized beam at 54° ; the OSCAT scatterometer on OceanSat-II also uses a similar configuration [14], [15]. The other main configuration for scatterometers is the fan beam type, such as SeaSAT [10], ERS-1/2 [16], NASA Scatterometer [9], and Advanced Scatterometer [17]. The fan beam type has consistent measurement geometry (azimuthal separation of looks per WVC) across the swath, whereas the pencil beam type has varying geometry across the swath and is poor in the nadir region and far swath. However, the fan beam type has a significantly narrower swath and has a “nadir gap,” whereas the pencil beam type images a very wide swath and has no gaps.

The wind retrieval processing involves three main steps: 1) a point-wise maximum-likelihood estimate of wind speed and wind direction, which typically has four ambiguities; 2) a median filter, which selects the best ambiguity; and 3) the directional interval retrieval (DIR) processing [18] step, which uses the directional spread of the objective function and allows the retrieved wind direction to vary within the region around

Manuscript received September 6, 2012; revised November 9, 2012; accepted December 7, 2012.

The authors are with the Jet Propulsion Laboratory, California Institute of Technology, Pasadena, CA 91109 USA (e-mail: Alexander.Fore@jpl.nasa.gov).

Digital Object Identifier 10.1109/TGRS.2012.2235843

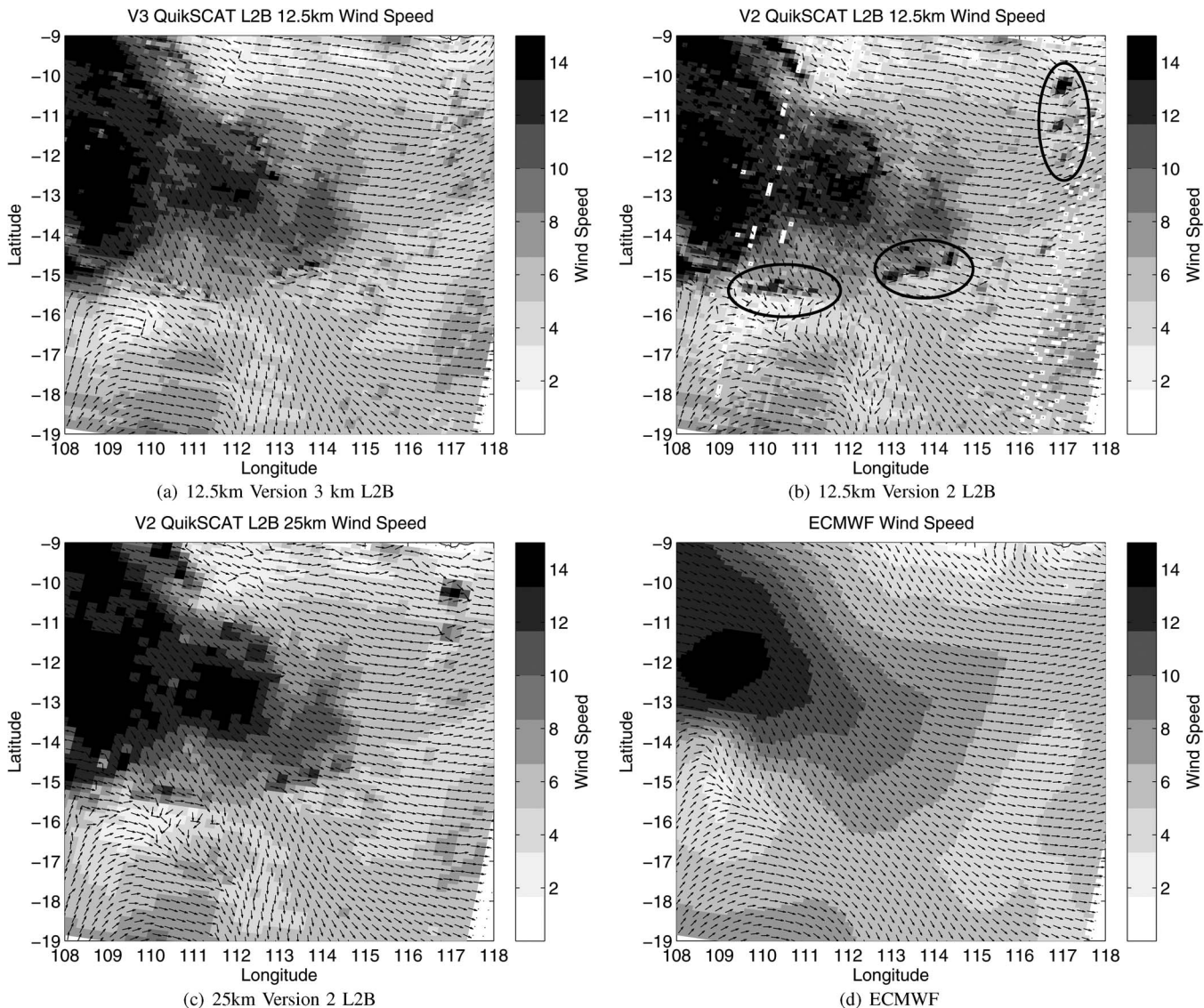


Fig. 1. (a) (In gray scale) QuikSCAT retrieved speed and (arrows) direction for the 12.5-km V3 L2B processing. (b) 12.5-km V2. (c) 25-km V2. (d) ECMWF. The two high-resolution retrievals have the arrows plotted at every other WVC in each of the cross-track and along-track dimensions. We have drawn ellipses around some regions of significant rain errors in the previous L2B12 processing in (b). These plots demonstrate the main improvements in the V3 12.5-km L2B data set, namely, less noise in the direction retrievals, the absence of gaps in the high-resolution retrievals, and (upper right corner of wind field) the removal of high wind speeds due to rain contamination.

the selected ambiguity. This final step allows us to further smoothen the wind retrievals in the regions where instrument performance is poor and significantly improves the final wind vector products.

In Section II, we give an overview of the various algorithm improvements included in this reprocessing. In Section III, we present the results of some validation studies comparing the performance of this product to the previous high-resolution QuikSCAT L2 product. In Section IV, we leverage the decade-long history of QuikSCAT observations and find no significant trend in wind speed.

II. ALGORITHM IMPROVEMENTS

The V3L2B12 OVW data product consists of wind retrievals based on a 12.5-km grid, which is the same as in the V2L2B12 12.5-km data product [5]. We begin with the same L1B data as used in the previous processing. We have introduced a

number of algorithm improvements, including changes at the L1B to L2A processing with binning improvements to enhance resolution, decrease noise, and reduce gaps in wind field. The L2A to L2B processing includes model function improvements, correction of rain contaminated speeds, and adjustments to the DIR thresholds. The post-L2B data processing includes a cross-track bias removal.

A. Level 1B To Level 2A Processing: Measurement Binning Improvement

The fundamental QuikSCAT measurements are backscatter “slices.” The data obtained within each 25 km \times 35 km antenna footprint are broken up by range to target into 25 km \times 7 km slices. The L1B to L2A processing of the slice σ_0 data begins with the assignment of every slice to a WVC. This is a crucial part of the wind vector processing, as it determines what observations are grouped together for wind retrieval. To obtain

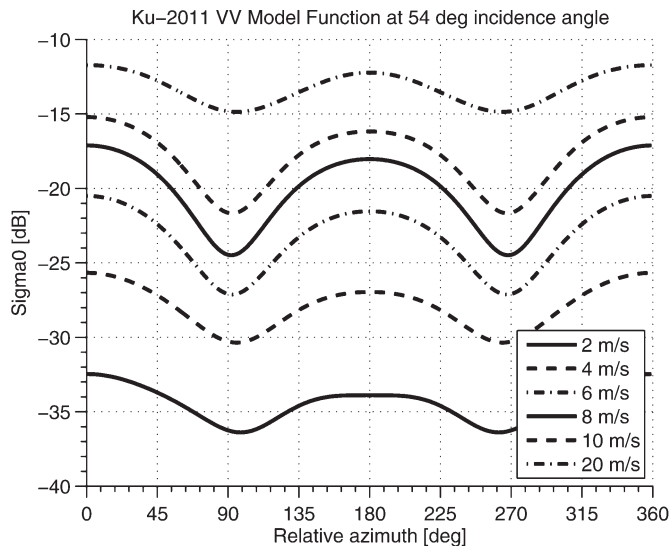


Fig. 2. Ku-2011 GMF for VV-polarization at 54° incidence angle. x -Axis is the relative azimuth angle between the wind and radar look directions. y -Axis is the σ_0 in decibels. The different curves are the GMFs for different wind speeds.

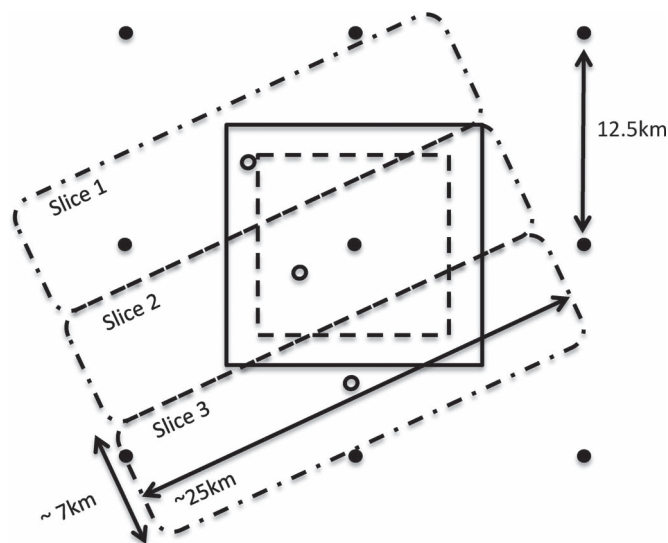


Fig. 3. Diagram of the L2A WVC grid and the three sequential slice observations. Filled dots are WVC centroids; circles are slice centroids. (Solid square) Extent of one WVC grid cell. (Dashed square) Overlap region. Dash-dot outline represents the nominal slice boundary used in the overlap algorithm.

a good wind solution, we need enough observations of sufficient quality for all available azimuths in each WVC.

In this reprocessing, we introduce a new gridding algorithm, i.e., the overlap algorithm. The previous processing uses what we refer to as the centroid algorithm, which places a given σ_0 slice measurement in a WVC if the centroid of the slice lies within that WVC. However, the overlap algorithm places a slice σ_0 in a WVC if any portion of the nominal slice footprint falls within the “overlap” region. In Fig. 3, we show a diagram of a WVC and an example of how the slices fall with respect to this WVC. The filled black dots represent the centers of WVCs, the solid line represents the nominal WVC boundaries, and the dashed line represents the “overlap” region. The circles represent the slice centroids, and the dash-dot lines represent the nominal slice boundaries. If the circle lies within the solid

box, then the slice is placed into that WVC when using the centroid algorithm; however, when using the overlap, we place a slice into a WVC if any portion of the area enclosed by the dash-dot line lies within the dashed line. An important point to note is that the overlap algorithm can result in a slice being assigned to multiple WVCs, whereas the centroid algorithm always assigns a slice to only one WVC. Overlap processing introduces some spatial correlation among the WVCs at the σ_0 level and results in a slight decrease in resolution.

After gridding, we composite all sequential slices from the same antenna footprint that are assigned into the same WVC into one L2A σ_0 observation. These observations are the inputs to wind retrieval processing. Generally, the new gridding algorithm results in an increased number of slices being assigned to the same WVC, which results in improved wind retrieval performance. In Fig. 4(a), we plot the average number of slices per composite and composites per WVC for the centroid and overlap algorithms. We see a significant increase in the composites per WVC versus cross-track index (CTI), which leads to improved wind retrieval performance. In Fig. 4(b), we plot the percentage of WVCs that do not have wind retrieval due to too few measurements in the V2L2B12 product on top and the V3L2B12 product on the bottom. We see a vast reduction in the percentage of WVCs that do not have wind retrieval when using the overlap processing, most noticeable near the center of the swath (CTI 76) and in the single-beam portions of the swath. The previous product had holes in these regions due to instrument geometry, and overlap gridding wholly mitigates this issue at the cost of a somewhat reduced resolution. Although the resolution is somewhat reduced by overlap gridding, wind retrieval error is significantly reduced. An important piece of evidence showing that this trade is favorable is that the accuracy of the V3L2B12 winds with respect to point wind estimates (buoys) are improved (see Fig. 11).

B. L2A to L2B Processing: DIR Thresholds

The V2L2B12 product contained significant direction noise, which impeded the computation of wind vector derivative products (divergence, curl, etc.). This noise is due to the direction computed in the DIR algorithm “hitting” the hard limits imposed by the 80% probability threshold value used to build the direction ranges [18]. In the V3L2B12 product, we have adjusted the DIR probability threshold from 80% to 99%. This results in a significant reduction in direction noise, as demonstrated in Fig. 6.

C. L2A to L2B Processing: Model Function

The V3L2B12 product uses a recently redeveloped model function for Ku-Band from Remote Sensing Systems, Ku2011, which is an improved version of the Ku2001 QuikSCAT model function [12]. Due to the long history of passive wind retrievals [e.g., Special Sensor Microwave Imager (SSM/I)] and the abundance of WindSAT/QuikSCAT matchups, WindSAT was used to retune the Ku2001 model function [7], [19]. This allows an intercalibrated record of ocean wind products from passive and active microwave remote sensing instruments. The new model function introduces a wind speed bias as compared with ECMWF and other numerical weather products (NWP). This

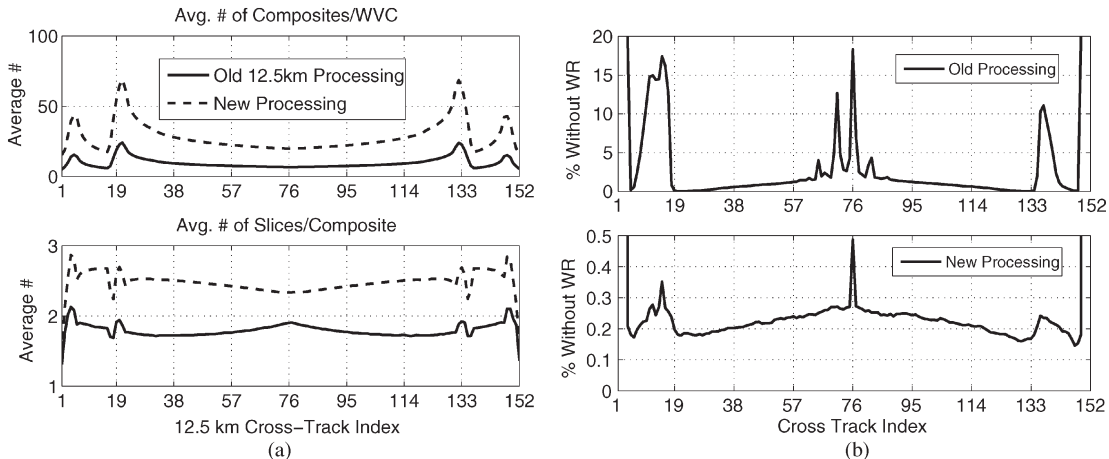


Fig. 4. (Top left) Average number of composites/WVC for the centroid (V2L2B12-solid line) and overlap gridding algorithms (V3L2B12-dashed line), both versus CTI. (Bottom left) Average number of slices/composite for the (solid line) V2 and (dashed line) V3 gridding methods versus CTI. (Top right) Percentage of WVCs without wind retrieval versus CTI for the V2L2B12 product (centroid gridding) and (bottom right) same for the V3L2B12 product (overlap gridding).

is because this GMF is tuned to buoys instead of being tuned to ECMWF, whereas the previous Ku2001 model function was tuned to ECMWF [12].

D. L2A to L2B Processing: Rain Flagging and Correction

The V3L2B12 product contains a rain flag, a rain impact quantity, and a rain-corrected speed. The rain flag is unchanged from the V2L2B12 product; however, both the rain impact and rain-corrected speed are new additions. The rain impact and rain-correction algorithm are based on an artificial neural network; in Fig. 5, we show a block diagram of the neural-network algorithm. The inputs to the neural network are the four flavors of σ_0 (fore HH, fore VV, aft HH, and aft VV), the first rank wind speed solution, and the cross-track distance [6]. We only perform this correction in the dual-beam portion of the swath, thus, no rain correction is estimated or applied in the outer swath. From the neural network, we estimate a rain impact quantity, which is meant to quantify the rain contamination level on that particular WVC. Whenever the rain impact quantity exceeds a threshold, we apply the rain speed correction and assign every ambiguity the same objective function value, indicating that the instrument does not have any skill in ranking ambiguities in rain.

E. Post-L2B Processing: Cross-Track Bias Correction

After the completion of L2B processing, we apply a final cross-track bias correction, which removes residual speed biases as a function of CTI. We first generate a table of speed bias, as compared with ECMWF as a function of retrieved wind speed and CTI for both rain-free and rainy conditions. Then, we create the correction table by subtracting from the computed speed bias for a given CTI and the retrieved speed for CTI 37 and 115 (in the so-called “sweet spot”). We perform this correction separately for rain-free and rainy observations. This way, we flatten the speed bias trend in the cross-track dimension; however, we do not remove the overall bias, as compared with ECMWF. ECMWF is only used as a reference OVW that does not have any cross-track dependence.

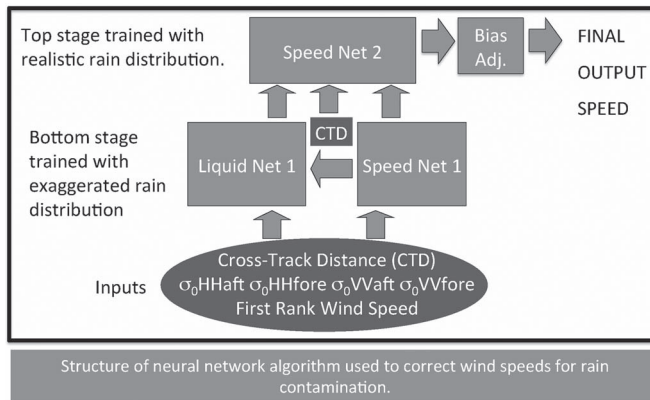


Fig. 5. Overview of the processing flow for the rain impact and correction algorithm. The inputs to the algorithm are the cross-track-distance, fore and aft σ_0^{HH} , fore and aft σ_0^{VV} , and the wind speed solution with the optimum objective function value.

III. VALIDATION

Here, we validate the V3L2B12 data product using data from all of year 2008; results from other years are nearly identical and not shown. One important application of OVW retrievals is for the generation of wind derivative products such as wind divergence, wind curl, wind stress divergence, and wind stress curl. The V2L2B12 product was not well suited to computation of these quantities due to the high levels of noise in the retrievals, which was particularly evident in the wind direction. In Fig. 6, we quantify the direction noise by comparing the cumulative distribution function (CDF) of the WVC absolute direction error, as compared with the surrounding 3×3 median filtered direction using all of year 2008¹ versus CTI. The previous processing has significant shot noise, giving rise to long tails in the CDF of the direction difference, particularly in the nadir region and single-beam swath. In the V3L2B12 product, the magnitude of the direction noise is reduced by a

¹Note that we are applying a vector median filter to the sines and cosines of the retrieved wind direction as opposed to filtering the direction itself.

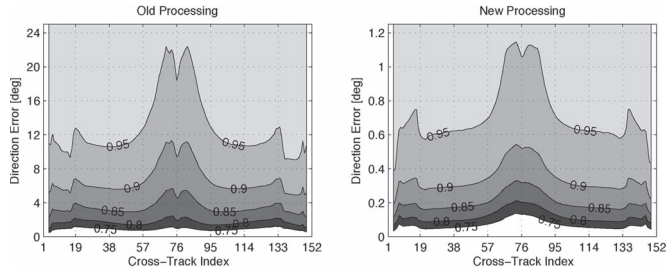


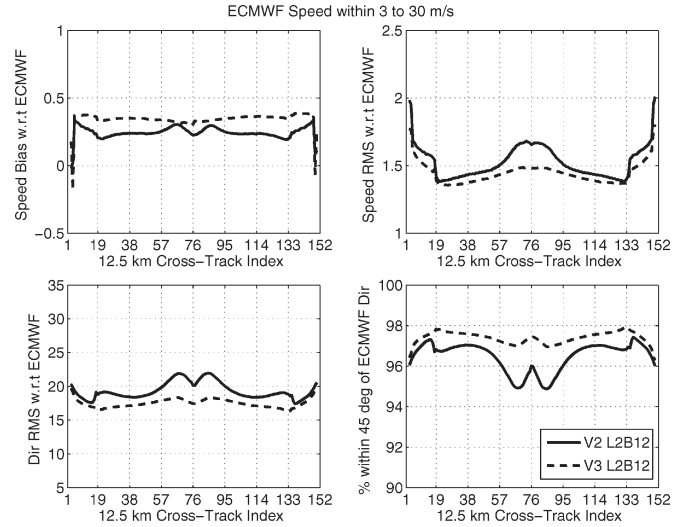
Fig. 6. (Left) CDF of the absolute difference between the retrieved direction and the surrounding 3×3 median filtered direction for the V2L2B12 product as a function of CTI. (Right) Same as the left but for the V3L2B12 product. The contour curves are at the 75%, 80%, 85%, 90%, and 95% CDF levels for both plots. Note the vastly reduced noise level in V3L2B12, in particular, there is a factor of 20 difference in the Y-scale of the two plots.

factor of 20—mostly due to the new gridding algorithm and changed DIR [18] thresholds.

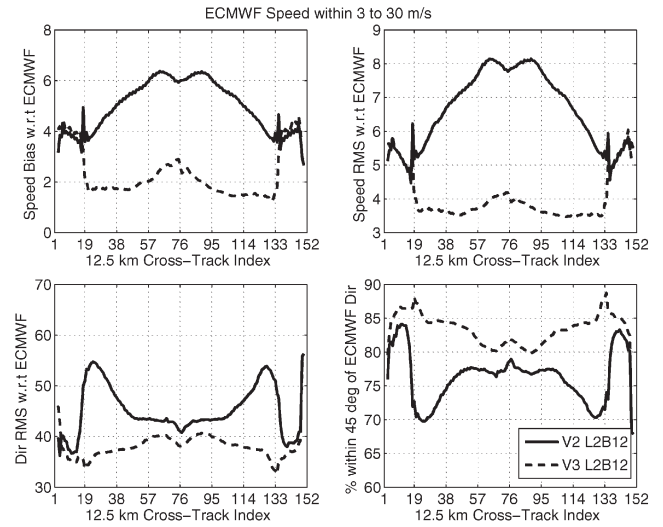
A. Comparison to NWP: ECMWF

In choosing a NWP to perform global validations against it, we have used ECMWF instead of National Centers for Environmental Prediction (NCEP) since we use the NCEP forecast product to seed the ambiguity removal process. In Fig. 7, we compute the speed mean difference in the upper left, speed root-mean-square (RMS) difference in the upper right, direction RMS difference in the lower left, and percentage of WVCs that have retrieved direction within 45° of ECMWF winds in the lower right for rain-free data. The V3L2B12 product has more mean difference, as compared with ECMWF than the V2L2B12 product; however, this is due to the model function and was not unexpected. Even with this moderate increase in the mean difference, the speed RMS difference has decreased, significantly indicating less noise in the new wind vector retrievals. In the direction RMS difference and percentage of WVCs within 45° of ECMWF, we note significant improvements in the V3L2B12 product. In Fig. 7(b), we plot the same for rain-flagged data. Note the very large reduction in the overall mean speed difference and RMS speed difference in the V3L2B12 product, as compared with the V2L2B12 product. We also see a significant improvement in the direction performance with the new rain algorithm. This is due to the equal treatment of the ambiguities during ambiguity removal processing regardless of the objective function value when the rain speed correction is applied.

In Fig. 8(a), we plot two-dimensional (2-D) log histograms of retrieved speed and direction versus ECMWF speed/direction for all rain-free observations in year 2008; in the upper right, we plot the V3L2B12 speed versus the ECMWF speed; in the upper left, we plot the V3L2B12 direction versus the ECMWF direction; and in the lower panel, we plot the same for the V2L2B12 product. Notice the reduction in erroneous high-wind speed retrievals where ECMWF has a low wind speed and the reduction in the tendency to retrieve cross-track wind directions in the V3L2B12 product. In Fig. 8(b), we plot the same for all rain-flagged data. In the V2L2B12 product, we see that rain contamination has introduced a large speed bias for low ECMWF wind speeds; in the V3L2B12 product, this effect is almost entirely mitigated. Another effect of rain contamination in the V2L2B12 product is the tendency for the retrieved wind



(a) Rain-Free Data; ECMWF Speed in 3,30



(b) Rain-Flagged Data; ECMWF Speed in 3,30

Fig. 7. (a) (Upper left) Speed mean difference. (Upper-right) Speed RMS difference. (Lower left) Direction RMS difference. (Lower right) Percentage of WVCs that have the wind retrieval within 45° of ECMWF winds. All statistics are computed with respect to triply interpolated ECMWF wind vectors, and we plot the new reprocessing as dashed lines and the V2L2B12 product as solid lines. We include only data flagged as rain free and data such that the collocated ECMWF wind speed is between 3 and 30 m/s. In (b), we plot the same for rain-flagged WVCs.

direction to lie in the cross-track direction, hence generally somewhat above and below $\pm 90^\circ$ relative north. While the V3L2B12 product also shows this tendency for wind retrievals to lie in the cross-track direction, the magnitude is somewhat reduced, and the histograms are more focused on the 1 : 1 line.

In Fig. 9, we plot the speed (on top) and direction (in the middle) mean and the standard deviation (STD) of the difference, as compared with ECMWF, as a function of SSMI rain rate for all SSMI/QuikSCAT matchups in 2008. On the bottom in Fig. 9, we plot the log histogram of the SSMI rain rate. The matchup criteria were 30 min in time and less than $1/4^\circ$ in latitude/longitude. We see a very significant improvement in the speed bias as compared with ECMWF in rainy conditions. The speed STD has also decreased; however, it is still large compared with rain-free conditions. We also note that the direction.

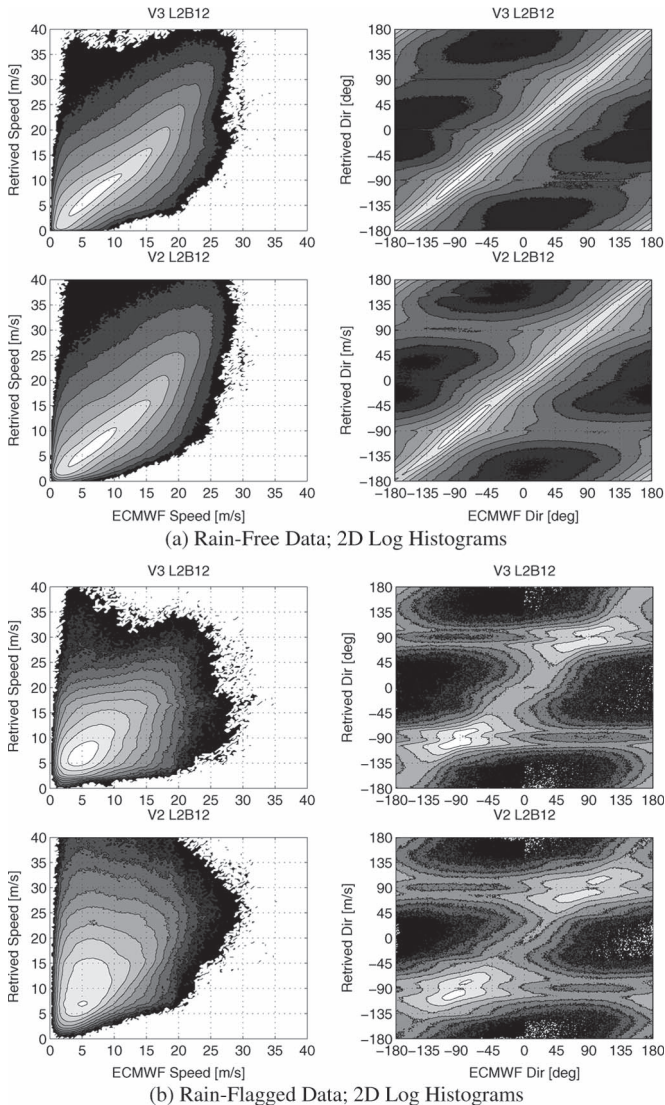


Fig. 8. (a) (Upper left) Two-dimensional log histogram of rain-free retrieved speeds compared with the ECMWF speed for the V3L2B12 product. (Lower left) Same for the V2L2B12 product. Note that lighter shades of gray indicate more counts. (Upper right) Two-dimensional log histogram for rain-free retrieved directions compared with the ECMWF direction for the V3L2B12 product. (Lower right) Same for the V2L2B12 product. In (b), we plot the same for rain-flagged WVCs. Notice the high wind speed bias has been removed and that the directional histogram has reduced tendency to retrieve directions that are cross-track.

B. Buoys

We have also performed extensive buoy validations of our new wind processing. We used buoys from the National Data Buoy Center, Pilot Research Moored Array in the Tropical Atlantic project, and Tropical Atmosphere Ocean/Triangle Trans-Ocean Buoy Network. In Fig. 10, we plot the locations and buoy type for all buoys used in this analysis.

The buoy observations were spatially and temporally collocated with QuikSCAT WVCs by using the nearest WVC to each buoy such that the WVC was within 12.5 km of the buoy, and the time difference was less than 30 min. Finally, we use the formalism presented in [20] to solve for the equivalent neutral wind speed at a 10-m height from the actual buoy speed and other *in situ* observations (water temperature, air temperature, etc.). The conversion from actual buoy wind speed to equivalent

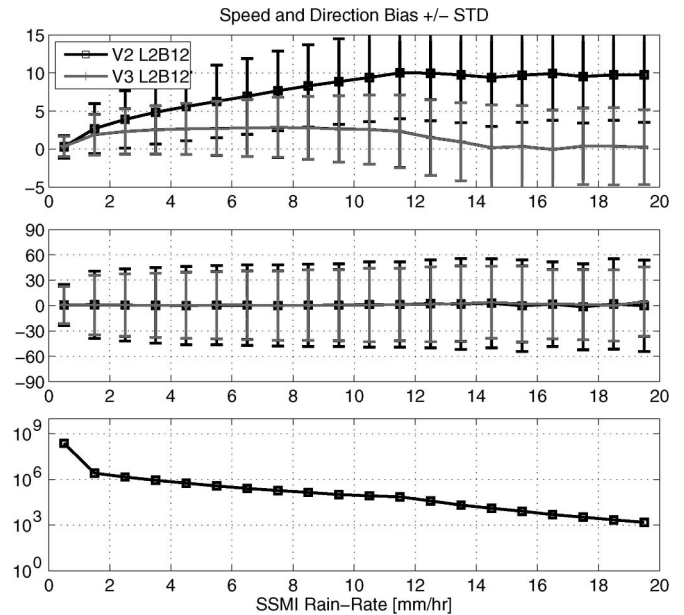


Fig. 9. (Top) Speed bias relative to ECMWF as a dashed line and the speed standard error deviation as plus/minus brackets about the bias. (Middle) Same for the direction error, as compared with ECMWF. (Bottom) Histogram of the SSMI rain rate. These statistics were generated from all QuikSCAT/SSMI matchups in year 2008, and all the statistics are done as a function of the SSMI rain rate. We show statistics for the V3L2B12 product in gray and for the V2L2B12 product in black.

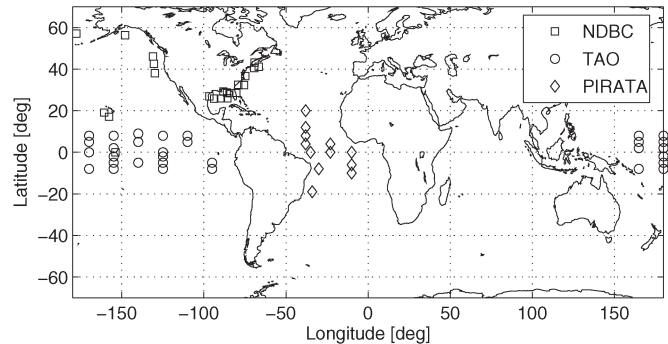


Fig. 10. Locations of buoys used in buoy analysis.

neutral wind speed involves a correction for anemometer height and for atmospheric stability [20].

Note that overall, the speed and direction STD has been reduced in the V3L2B12 product, except for perhaps the speed STD for speeds less than 2 m/s. In [21], an extensive buoy validation was performed for the 25-km data product, and it was shown that the DIR retrievals had an RMS speed error of 1.01 m/s and an RMS direction error of 22.4° for buoy speeds greater than 3 m/s. In Fig. 11, we plot the speed bias and STD with respect to the buoy wind speed on top, the direction bias and STD in the middle, and the histogram of buoy wind speeds on the bottom. This plot includes all buoys from year 2008. We see that for the new product, the overall speed RMS difference is 1.01 m/s, and the direction RMS difference is 17.4°.

C. Spectral Characteristics of V3L2B12 Product and V2L2B12 Product

From turbulence theory, we expect a k^α power-law scaling in the kinetic energy spectra, and consistent results have been

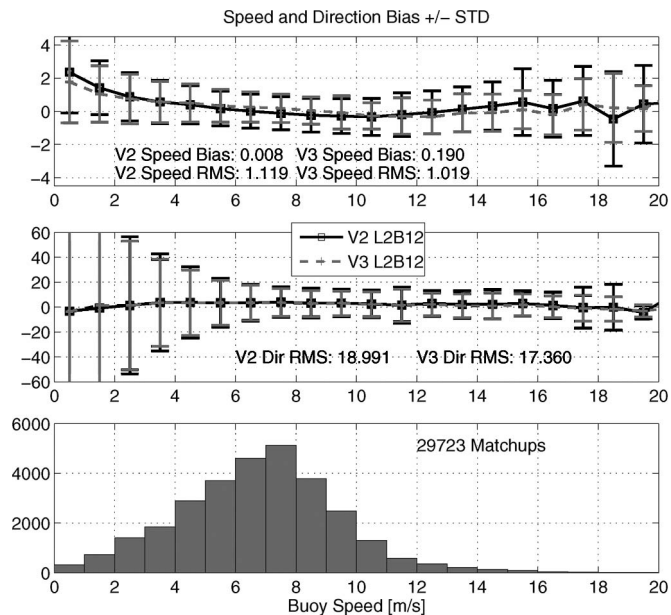


Fig. 11. (Top) QuikSCAT speed bias as compared with buoy speed and the QuikSCAT speed standard deviation as plus/minus brackets about this line. In black, we plot the V2L2B12 product, and in gray, we plot the V3L2B12 product. (Middle) Same for the direction error, as compared with buoy direction. (Bottom) Histogram of the buoy speeds. These statistics were generated from all buoy matchups in year 2008 and that are done as a function of the buoy speed. We show statistics for the V3L2B12 product in gray and for the V2L2B12 product in black. These matchups include only data that have been flagged as rain free. The overall statistics inset in plots have been computed using only buoy matchups where the buoy speed was greater than 3 m/s.

obtained from numerous spaceborne scatterometers, which show that there is a power-law scaling of 1.8 to 2.2 [22], [23]. In Fig. 12, we plot the speed spectra and the spectra of the direction phasor as a function of the wavelength for the V3L2B12 and V2L2B12 products. As the wavelength decreases, we see that the V2L2B12 product's spectra show significantly more "flattening" (spectral slope becomes more flat) than the V3L2B12 product. Since we expect power-law behavior down to scales on the order of 1 km, this deviation from the power law indicates additional noise in the wind vector product due to instrument limitations and processing [Rodríguez and Chau, unpublished]. Both speed and direction spectra of the V2L2B12 product begin to deviate from the power law near the 200-km wavelength, whereas the V3L2B12 product flattens near 100 km for the direction and 40 km for the speed. The reduction in spectral "flattening" at smaller wavelengths significantly indicates less small-wavelength noise in the V3L2B12 speeds and directions, as compared with the V2L2B12 product.

The new processing algorithms have also reduced cross-track dependent distortion of the spectra. In Fig. 13, we show a contour plot of the spectra versus CTI and frequency, with the speed spectra of the V2L2B12 product in the upper left, that of the V3L2B12 product in the upper right, the direction spectra² of the V2L2B12 product in the lower left, and that of the new product in the lower right. The plots for the V2L2B12 speed spectra have the same contour levels and color scaling as those for the V3L2B12 speed spectra, and the same is true for the direction spectra plots. Notice that the V3L2B12 product

²We compute the spectra of the phasor.

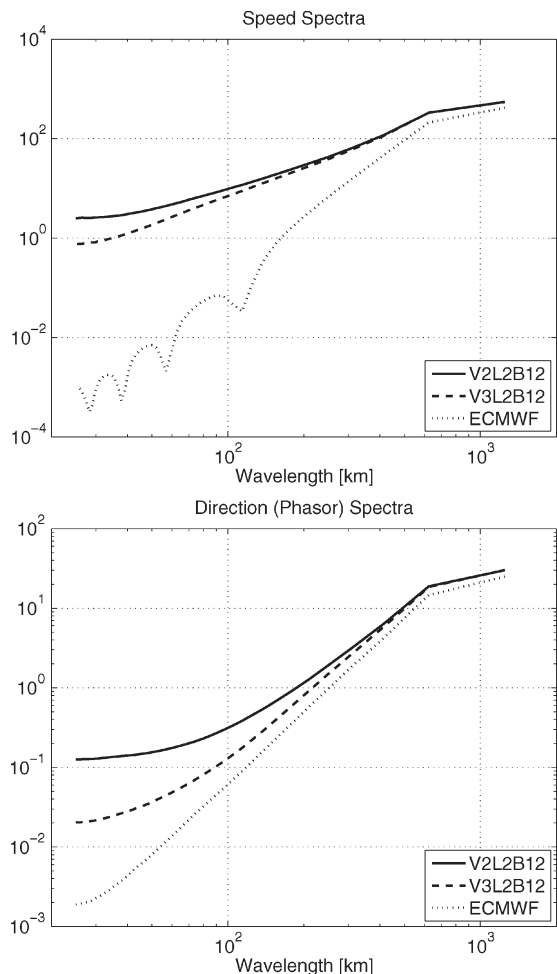


Fig. 12. (Top) Speed spectra for cross-track locations (21-51 and 101-123) for the V2L2B12 product, the V3L2B12 product, and ECMWF that has been interpolated to the WVC locations and times. (Bottom) Direction (phasor) spectra for the same.

has a smaller white noise floor as indicated by more contour levels and lighter shade as the frequency increases. In addition, the V3L2B12 product shows less cross-track distortion of the spectra contour levels, indicating improved performance in the nadir region and far swath.

IV. TRENDS IN QUIKSCAT OVW OVER MISSION

In Fig. 14, we plot the monthly averages for the V3 and V2L2B12 products as a function of time for the ten-year QuikSCAT mission. We compute a linear fit and find that there is a very small -2.83 cm/s/decade trend in the retrieved wind speed. However, given the accuracy of the QuikSCAT instrument, we do not believe this trend is significantly different from zero. In [24], the authors found an 8 cm/s/decade trend in the SSM/I data set, and in [25], (also see [26] and [27]) a larger trend was found.

V. SUMMARY

The newly introduced gridding algorithm improvements have been shown to offer a very significant improvement in the quality and utility of the 12.5-km QuikSCAT wind vectors.

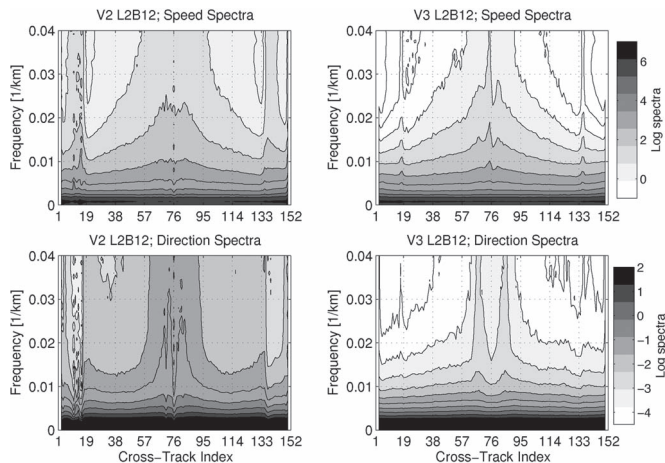


Fig. 13. (Upper left) Contour plot of the speed spectra versus CTI and frequency for the V2L2B12 product. (Upper right) Same for the V3L2B12 product. (Lower left) Direction spectra for the V2L2B12 product. (Lower right) Same for the V3L2B12 product. The color bars and contour levels for both speed spectra plots are identical as are those for the direction spectra.

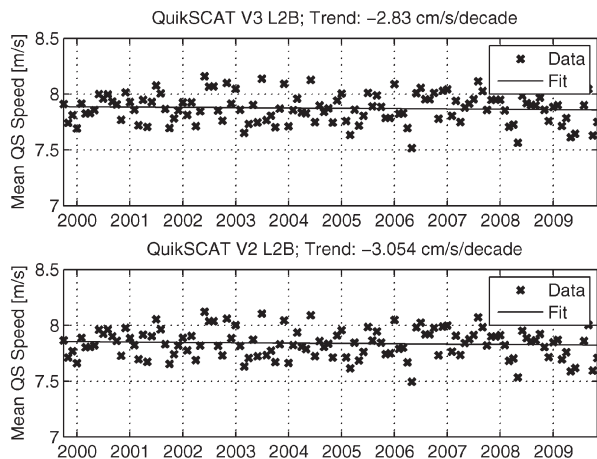


Fig. 14. (Top) Average QuikSCAT speed in the V3L2B12 product. (Bottom) Same for the V2L2B12 product. Each data point is an average over all rain-free observations for one month. We see that QuikSCAT has a trend of -2.83 cm/s per decade.

We have demonstrated that the new gridding algorithm results in far less WVCs lacking wind retrievals, i.e., 2.6% for the V2L2B12 product versus 0.22% for the V3L2B12 product.³ In addition, the new gridding algorithm and adjustments to the DIR processing have resulted in a direction field with far less noise than before; in particular, we have reduced the occurrence of “shot” noise by a factor of 20. This reduction in noise greatly improves the utility of the retrieved winds for computing wind derivative products (divergence, curl, stress divergence, and stress curl). We have compared our retrievals to ECMWF, buoys, and SSMI and all show a significant reduction in the RMS speed and direction (excluding SSMI) errors. The RMS speed errors, as compared with ECMWF for rain-free data, have been decreased from 1.52 to 1.44 m/s overall and the RMS direction errors from 19.39° to 17.48° . The overall speed RMS difference, as compared with buoys, has decreased from 1.12 to

1.02 m/s, and the direction RMS difference has decreased from 18.99° to 17.36° .

The quality of our data in rain, as assessed using buoys and ECMWF, is greatly improved by a new neural-network-based rain correction [6]. As compared with ECMWF, the speed RMS difference has decreased from 7 to 3.8 m/s. Using spectral methods, we show that the direction resolution of the V3L2B12 product is improved due to the significantly reduced direction noise. We show that the cross-track variation in spectral performance has also improved from the previous processing. Finally, we have shown that QuikSCAT has given stable estimates of OVW for over a decade.

ACKNOWLEDGMENT

This work was carried out at the Jet Propulsion Laboratory, California Institute of Technology under a contract with the National Aeronautics and Space Administration.

REFERENCES

- [1] Y. Zhao, A. Liu, and D. Long, “Validation of sea ice motion from QuikSCAT with those from SSMI and buoy,” *IEEE Trans. Geosci. Remote Sens.*, vol. 40, no. 6, pp. 1241–1246, Jun. 2002.
- [2] I. Mladenova, V. Lakshmi, J. Walker, D. Long, and R. De Jeu, “An assessment of QuikSCAT Ku-band scatterometer data for soil moisture sensitivity,” *IEEE Geosci. Remote Sens. Lett.*, vol. 6, no. 4, pp. 640–643, Oct. 2009.
- [3] A. Bartsch, R. A. Kidd, W. Wagner, and Z. Bartalis, “Temporal and spatial variability of the beginning and end of daily spring freeze/thaw cycles derived from scatterometer data,” *Remote Sens. Environ.*, vol. 106, no. 3, pp. 360–374, Feb. 2007.
- [4] A. Bartsch, “Ten years of SeaWinds on QuikSCAT for snow applications,” *Remote Sens.*, vol. 2, no. 4, pp. 1142–1156, Apr. 2010.
- [5] R. S. Dunbar, T. Lungu, B. Weiss, B. Stiles, J. Huddleston, P. Callahan, G. Shirliffé, K. Perry, C. Hsu, C. Mears, F. Wentz, and D. Smith, *QuikSCAT Science Data Product User’s Manual*. Pasadena, CA: Jet Propulsion Laboratory, Sep. 2006.
- [6] B. Stiles and R. Dunbar, “A neural network technique for improving the accuracy of scatterometer winds in rainy conditions,” *IEEE Trans. Geosci. Remote Sens.*, vol. 48, no. 8, pp. 3114–3122, Aug. 2010.
- [7] L. Ricciardulli and F. Wentz, “Reprocessed QuikSCAT (V04) wind vectors with Ku-2011 geophysical model function,” in *Remote Sens. Syst.*, Santa Rosa, CA, USA, Apr. 2011. [Online]. Available: http://www.ssmi.com/qsat/qsat_Ku2011_tech_report.pdf
- [8] W. J. Plant, “A two-scale model of short wind-generated waves and scatterometry,” *J. Geophys. Res.*, vol. 91, no. C9, pp. 10735–10749, Jan. 1986.
- [9] F. Naderi, M. Freilich, and D. Long, “Spaceborne radar measurement of wind velocity over the ocean—an overview of the NSCAT scatterometer system,” *Proc. IEEE*, vol. 79, no. 6, pp. 850–866, Jun. 1991.
- [10] W. L. Jones, L. C. Schroeder, D. H. Boggs, E. M. Bracalente, R. A. Brown, G. J. Dome, W. J. Pierson, and F. J. Wentz, “The SEASAT-A satellite scatterometer: The geophysical evaluation of remotely sensed wind vectors over the ocean,” *J. Geophys. Res.*, vol. 87, no. C5, pp. 3297–3317, Apr. 1982.
- [11] L. Schroeder, P. Schaffner, J. Mitchell, and W. Jones, “AAFE RADSCAT 13.9-GHz measurements and analysis: Wind-speed signature of the ocean,” *IEEE J. Ocean. Eng.*, vol. OE-10, no. 4, pp. 346–357, Oct. 1985.
- [12] F. Wentz and D. Smith, “A model function for the ocean-normalized radar cross section at 14 GHz derived from NSCAT observations,” *J. Geophys. Res.—Oceans*, vol. 104, no. C5, pp. 11499–11514, Jan. 1999.
- [13] H. Hersbach, A. Stoffelen, and S. de Haan, “An improved C-band scatterometer ocean geophysical model function: CMOD5,” *J. Geophys. Res.*, vol. 112, no. C3, p. C03006, Mar. 2007.
- [14] B. Gohil, P. Sharma, R. Sikhakolli, and A. Sarkar, “Directional stability and conservation of scattering (DiSCS)-based directional-ambiguity removal algorithm for improving wind fields from scatterometer: A QuikSCAT example,” *IEEE Geosci. Remote Sens. Lett.*, vol. 7, no. 3, pp. 592–595, Jul. 2010.

³Excluding 3 WVCs of each side of the swath.

- [15] B. Gohil, A. Sarkar, and V. Agarwal, "A new algorithm for wind-vector retrieval from scatterometers," *IEEE Geosci. Remote Sens. Lett.*, vol. 5, no. 3, pp. 387–391, Jul. 2008.
- [16] E. Attema, "The active microwave instrument on-board the ERS-1 satellite," *Proc. IEEE*, vol. 79, no. 6, pp. 791–799, Jun. 1991.
- [17] J. Figa-Saldaña, J. J. Wilson, E. Attema, R. Gelsthorpe, M. R. Drinkwater, and A. Stoffelen, "The advanced scatterometer (ASCAT) on the meteorological operational (MetOp) platform: A follow on for European wind scatterometers," *Can. J. Remote Sens.*, vol. 28, no. 3, pp. 404–412, Jun. 2002.
- [18] B. Stiles, B. Pollard, and R. Dunbar, "Direction interval retrieval with thresholded nudging: A method for improving the accuracy of QuikSCAT winds," *IEEE Trans. Geosci. Remote Sens.*, vol. 40, no. 1, pp. 79–89, Jan. 2002.
- [19] T. Meissner, L. Ricciardulli, and F. Wentz, "All-weather wind vector measurements from intercalibrated active and passive microwave satellite sensors," in *Proc. IEEE Int. Geosci. Remote Sens. Symp.*, Jul. 2011, pp. 1509–1511.
- [20] T. Liu and W. Tang, "Equivalent Neutral Wind," Jet Propulsion Lab., Pasadena, CA, USA, Tech. Rep., Aug. 1996.
- [21] N. Ebuchi, H. C. Graber, and M. J. Caruso, "Evaluation of wind vectors observed by QuikSCAT/SeaWinds using ocean buoy data," *J. Atmos. Ocean. Technol.*, vol. 19, no. 12, pp. 2049–2062, Dec. 2002.
- [22] M. H. Freilich and D. B. Chelton, "Wavenumber spectra of pacific winds measured by the SEASAT scatterometer," *J. Phys. Oceanogr.*, vol. 16, no. 4, pp. 741–757, Apr. 1986.
- [23] J. Patoux and R. Brown, "Spectral analysis of QuikSCAT surface winds and two-dimensional turbulence," *J. Geophys. Res.—Atmos.*, vol. 106, no. D20, pp. 23995–24005, Jan. 2001.
- [24] F. J. Wentz, L. Ricciardulli, K. Hilburn, and C. Mears, "How much more rain will global warming bring?" *Science*, vol. 317, no. 5835, pp. 233–235, Jul. 2007.
- [25] I. R. Young, S. Zieger, and A. V. Babanin, "Global trends in wind speed and wave height," *Science*, vol. 332, no. 6028, pp. 451–455, Apr. 2011.
- [26] F. J. Wentz and L. Ricciardulli, "Comment on "Global trends in wind speed and wave height" ," *Science*, vol. 334, no. 6058, p. 905, Nov. 2011.
- [27] I. R. Young, A. V. Babanin, and S. Zieger, "Response to comment on "Global trends in wind speed and wave height" ," *Science*, vol. 334, no. 6058, p. 905, Nov. 2011.



Alexander G. Fore received the A.B. degree in physics from Vassar College, Poughkeepsie, NY, USA, in 2002 and the M.S. and Ph.D. degrees in physics from Carnegie Mellon University, Pittsburgh, PA, USA, in 2004 and 2008, respectively.

His doctoral work was modeling of complex fluids using the Lattice Boltzmann method. In March 2008, he joined the Radar Science and Engineering Section, Jet Propulsion Laboratory (JPL), Pasadena, CA, USA. At JPL, he has been working primarily on scatterometry, both forward modeling of the radar observation, as well as the retrieval of the geophysical quantity from the radar observation. He also has experience in synthetic aperture radar processing and calibration algorithms.



Bryan W. Stiles received the Ph.D. degree in electrical engineering from the University of Texas at Austin, Austin, TX, USA, in 1997.

His dissertation described mathematical structures based upon biological neural networks that are useful for modeling nonlinear spatiotemporal systems. From 1997 to the present time, he has been with National Aeronautics and Space Administration (NASA), Jet Propulsion Laboratory (JPL), Pasadena, CA, USA. At JPL, he has developed simulations, ground processing, and data analysis algorithms for spaceborne radar. He has worked on the end-to-end simulation of ocean wind scatterometers and developed algorithms for estimating winds and rain from Earth-orbiting scatterometer data. He developed a means for improving the wind retrieval accuracy of pencil beam scanning scatterometers that is employed today by NASA and National Oceanic and Atmospheric Administration in processing data from the QuikSCAT and OceanSAT-2 satellites. He also developed a statistical model of the impact of rain on ocean wind scatterometer data that is used to flag for rain contamination and correct ocean winds. As a member of the NASA Ocean Vector Winds Science Team, he has developed methods for improving the accuracy of scatterometer winds in hurricanes. In addition to his work with Earth observing radar, he also led the development of the synthetic aperture radar (SAR) processor for the Cassini radar instrument and developed methods for determining the surface height and spin parameters of Titan, which is Saturn's largest moon from the Cassini Radar data. He has produced SAR imagery of Titan that has appeared on the covers of *Science* and *Nature*. He has worked on spaceborne radar systems for 15 years and Cassini radar for 10 years.



Alexandra H. Chau received the B.S., M.S., and Ph.D. degrees from Massachusetts Institute of Technology, Cambridge, MA, USA, in 2002, 2004, and 2009, respectively, all in mechanical engineering.

Her graduate work focused on intracoronary Raman spectroscopy for characterizing atherosclerosis. Since 2009, she has been a Member of the Technical Staff with the Jet Propulsion Laboratory, California Institute of Technology, Pasadena, CA, USA, where she works on scatterometry, landing radars, and polarimetric synthetic aperture radar systems.



Brent A. Williams received the B.S. degree in electrical engineering from Brigham Young University, Provo, UT, USA, in 2005 and the Ph.D. degree in electrical engineering from Brigham Young University in 2010 with a specialization in high resolution ocean wind vector scatterometry and σ^0 reconstruction.

He is currently with the Jet Propulsion Laboratory, California Institute of Technology, Pasadena, CA, USA, continuing research in scatterometry, as well as other radar applications.

R. Scott Dunbar, photograph and biography not available at the time of publication.

Ernesto Rodríguez is with the Jet Propulsion Laboratory, California Institute of Technology, Pasadena, CA, USA, where has worked on radar interferometry, altimetry, scatterometry, scattering, and remote sensing algorithms. He is currently a Project Scientist for the QuikSCAT mission and a Payload Scientist for the SWOT mission.